Linear excitation schemes for IR planar-induced fluorescence imaging of CO and CO_2

Brian J. Kirby and Ronald K. Hanson

A detailed discussion of linear excitation schemes for IR planar-induced fluorescence (PLIF) imaging of CO and CO_2 is presented. These excitation schemes are designed to avoid laser scattering, absorption interferences, and background luminosity while an easily interpreted PLIF signal is generated. The output of a tunable optical parametric amplifier excites combination or overtone transitions in these species, and InSb IR cameras collect fluorescence from fundamental transitions. An analysis of the dynamics of pulsed laser excitation demonstrates that rotational energy transfer is prominent; hence the excitation remains in the linear regime, and standard PLIF postprocessing techniques may be used to correct for laser sheet inhomogeneities. Analysis of the vibrational energy-transfer processes for CO show that microsecond-scale integration times effectively freeze the vibrational populations, and the fluorescence quantum yield following nanosecond-pulse excitation can be made nearly independent of the collisional environment. Sensitivity calculations show that the single-shot imaging of nascent CO in flames is possible. Signal interpretation for CO_2 is more complicated, owing to strongly temperature-dependent absorption cross sections and strongly collider-dependent fluorescence quantum yield. These complications limit linear CO_2 IR PLIF imaging schemes to qualitative visualization but indicate that increased signal level and improved quantitative accuracy can be achieved through consideration of laser-saturated excitation schemes. © 2002 Optical Society of America

OCIS codes: 300.2530, 300.6340, 110.3080, 260.2510

1. Introduction

IR planar laser-induced fluorescence (PLIF)[1,2] is an imaging diagnostic in which infrared laser light is tuned spectrally to a molecular absorption line, shaped geometrically into a thin sheet, and used to excite vibrational transitions in the selected IR-active species in the illuminated plane. An infrared camera captures an image of the resulting vibrational fluorescence, interrogating the two-dimensional distribution of molecular concentration and providing information that can be used to explore reaction or mixing. IR PLIF is a modification of more traditional PLIF measurements[3] in that visible or UV excitation of electronic transitions is replaced by IR excitation of vibrational transitions. Since IR PLIF measurements can generate high signal levels that scale linearly with both laser energy and species concentration, IR PLIF has advantages over Raman[4] and multiphoton PLIF[5–7] for the imaging of species that lack convenient UV transitions.

Recent experimental efforts have demonstrated the ability of IR PLIF techniques to image CO[1,2] and CO_2.[2] An example result is shown in Fig. 1, demonstrating the quality of image that is achievable with use of this technique. However, previous efforts have not presented a detailed investigation of excitation schemes, the attendant energy-transfer processes, and the effects of both on the interpretation of IR PLIF signal. Specifically, there has been no thorough discussion to date of temperature and bath gas dependence in combustion flows. This paper thus complements previous imaging demonstrations by exploring the detailed collision dynamics for a variety of concentration-imaging schemes and presenting a model-based framework for interpreting current and future IR PLIF imaging efforts. Although PLIF imaging has been employed for visualization of a variety of flow parameters, including species concentration,[8] temperature,[9] pressure,[10] and reaction rate,[11] this paper will be structured solely around the imaging of molecular concentration; extensions to

When this research was performed, the authors were with the Department of Mechanical Engineering, Stanford University, Stanford, California 94309. B. J. Kirby (bjkirby@sandia.gov) is now with the Department of Microfluidics, Sandia National Laboratories, P.O. Box 969, Mail Stop 9951, Livermore, California 94551.

Received 20 February 2001; revised manuscript received 16 July 2001.

0003-6935/02/061190-12$15.00/0

© 2002 Optical Society of America

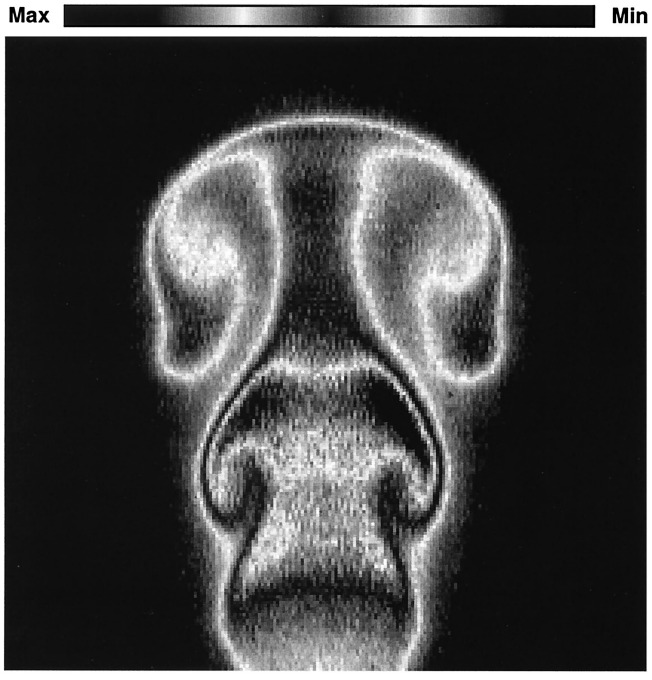

Fig. 1. Sample IR PLIF visualization of a room-temperature, 6-mm-diameter forced CO_2 jet mixing with ambient air. A single 8-mJ pulse at 2.0 μm pumps the $(20^01)_{II} \leftarrow (00^00)$ transition in CO_2, and an InSb camera collects fluorescence at 4.3 μm.

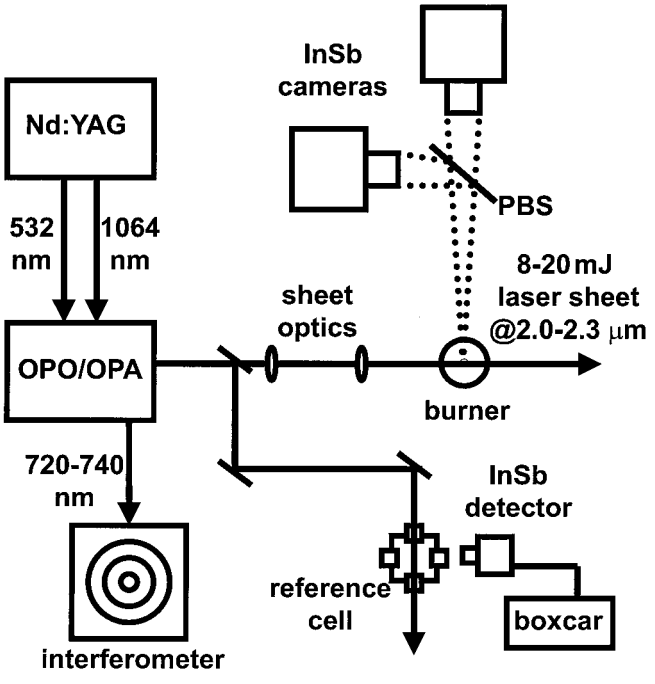

Fig. 2. Typical IR PLIF experimental setup. PBS, pellicle beamsplitter.

other flow parameters have been discussed in various reviews.[3,12,13]

The transition from basic demonstrations to applied combustion flows will require that excitation schemes be designed to maximize signal while minimizing error sources such as laser scatter, laser attenuation, radiative trapping, or spatially nonuniform fluorescence quantum yield. Since the processes of laser pumping, energy transfer, and camera integration change when PLIF techniques are modified to employ vibrational transitions, the analysis of these processes must be reconsidered for linear IR PLIF measurements. This paper presents the framework for analysis of IR PLIF excitation schemes as well as specific results for CO and CO_2. Later sections will describe typical experimental configurations and techniques for image postprocessing and interpretation. Following this, a section will present the excitation schemes being considered. Finally, a section will describe the pulsed excitation process, the parametric dependences of the effective fluorescence quantum yield, and the sensitivity of IR PLIF imaging techniques. The discussion will be structured first around CO; later sections will repeat this structure for CO_2. The analysis reveals challenges that are associated with the linear excitation of CO_2 and motivates investigation of laser-saturated infrared excitation of CO_2, which is experimentally demonstrated in a separate paper.[14]

2. Experimental Setup and Techniques

A typical experimental setup is shown in Fig. 2 to provide context for several of the experimental issues that are addressed through calculations later in this paper. Laser light that is resonant with vibrational transitions of CO or CO_2 is generated by a nanosecond-pulse, wavelength-tunable infrared laser source.[2] This optical parametric oscillator/amplifier(OPO/OPA) system tunes from 1.3 to 4.7 μm and generates 400-MHz linewidth pulses with energies as high as 20 mJ near the OPA degeneracy (2.1 μm). The beam is shaped with use of CaF_2 optics to form either a waist for single-point laser-induced fluorescence (LIF) measurements or a thin sheet for PLIF imaging. IR LIF signal is collected onto one or two 256 × 256 InSb cameras (Santa Barbara Focalplane, SBF 134). These cameras have been designed to provide short exposure times, and they are capable of submicrosecond exposures without detector bias changes or other temporally nonlinear effects that are common to most IR cameras. The LN_2-cooled InSb cameras are sensitive from 1.0 to 5.3 μm, with quantum efficiencies ranging from 85 to 95%.

Image postprocessing eliminates a variety of error sources.[1,3,15] Individual pixel responsivity and collection efficiency are calibrated with use of images of graybody emitters at different temperatures, and an online correction is applied to the measured signal. Background generated by analog-to-digital offsets or nonlaser-induced emission is corrected by subtracting the background (collected without laser excitation) from the image. A dual-camera setup and a pellicle beamsplitter[2] are used, when needed, to achieve real-time background subtraction in unsteady flows. We corrected for inhomogeneities in the incident laser sheet by recording fluorescence

from a uniform flow or laser scatter off a surface, binning along the direction of laser propagation, filtering out spatial frequencies in the image data that are greater than 10 cm^{-1}, and using the resulting function to normalize image data. No evidence of higher spatial frequencies ($k_x > 10\ cm^{-1}$) is observed in our laser sheet, so this filtering technique minimizes the noise that is introduced by sheet correction without generating a measurable error. We corrected for laser sheet inhomogeneity that is caused by minor laser attenuation in the imaged region by using known absorption cross sections.

3. Fluorescence Equation

The fluorescence equation for linear excitation can be written as

$$S_{f,\mathrm{lin}} = N_{p,\mathrm{inc}} n_{\mathrm{abs}} \sigma \ell \phi \eta_c \qquad (1)$$

where $S_{f,\mathrm{lin}}$ is the fluorescence signal in photons, $N_{p,\mathrm{inc}}$ is the number of photons incident on the imaged voxel, n_{abs} and σ are the number density and absorption cross section of the interrogated species, l is the voxel length, ϕ is the fluorescence quantum yield, and η_c is the efficiency of the collection optics. This form provides insight into the effect of experimental parameters on fluorescence signal. $N_{p,\mathrm{inc}}$ is dictated by laser pulse energy, η_c and l by the collection optics and camera, $n_{\mathrm{abs}}\sigma$ by the absorption properties of the interrogated species, and ϕ by the magnitudes of excited-state emission rates and the collisional interaction between the interrogated species and its environment. In particular, ϕ embodies the effects of vibrational energy-transfer (VET) processes with the bath gas. Fluorescence images can be converted to molecular concentration by way of Eq. (1) through the experimental removal of nonuniformities in $N_{p,\mathrm{inc}}$ (through sheet correction) and η_c (through pixel calibration), and the employment of excitation schemes that generate a nearly uniform value for $\sigma\phi$.

A. CO Excitation Schemes

The excitation scheme used for CO is designed to isolate the CO species concentration from other parameters and error sources (most notably spatial or thermal variations in σ and ϕ_{lin}) such that signal interpretation is straightforward. 8–15 mJ of energy is used to excite a rotational line of the first overtone ($2 \leftarrow 0$) band near 2.35 μm, and fundamental emission ($2 \rightarrow 1$, $1 \rightarrow 0$) is collected at 4.7 μm. The overtone absorption band is used so that laser scatter may be rejected with filters. In addition, absorption interferences are negligible in the 2.35-μm region except for a number of CO lines that overlap with CH_4 $\nu_3 + \nu_4$ band absorption lines; these lines should be avoided when methane flames are imaged. Fluorescence at 4.7 μm is collected, since 4.7 is the strongest spectral feature. Bandpass interference filters are used to minimize soot and water emission and to eliminate laser scatter and CO_2 emission. In flame experiments, a cold gas filter[16–18] is used to reduce emission associated with ($1 \rightarrow 0$) transitions, which is the primary component of the background emission from hot CO. Since most of the LIF from nascent CO at flame conditions occurs between excited states ($2 \rightarrow 1$), this filter effectively passes LIF and rejects flame luminosity.

Since laser excitation occurs on nanosecond time scales and fluorescence integration occurs on microsecond timescales, the pulsed excitation process can be considered temporally separate from the vibrational relaxation process. Calculations of absorption and fluorescence are hence presented in two different sections to follow.

1. Absorption

Equation (1) tacitly assumes that the laser-induced perturbation of state distributions is small, so the absorption cross section per CO molecule σ does not change during the laser pulse. The confirmation of this assumption establishes that S_f is linear with $N_{p,\mathrm{inc}}$ and that Eq. (1) may be used accordingly to interpret IR PLIF images. For the CO excitation scheme, experimental measurements and calculations of rotational energy-transfer (RET) processes during the laser pulse have been used to confirm that standard PLIF experimental techniques and postprocessing procedures [which assume that Eq. (1) is applicable] may be used. These procedures, which include the sheet-correction techniques described earlier in this section, can introduce errors if fluences are high enough to perturb state distributions and generate nonlinear absorption. By establishing that fluorescence is in the linear regime, we confirm with these absorption results the accuracy of current imaging experiments and can use the results to project the success of future efforts that might employ more powerful laser systems, different sheet optics, or irradiated regions of different sizes.

In this section, we model the pulsed excitation process by using a rate-equation analysis that includes the effects of both laser pumping and collisional rotational energy-transfer processes. Because vibrational energy transfer (VET) for CO is much slower than RET, VET is ignored during the laser pulse. Each rotational state j is considered (m_j states, though, are not distinguished). State-to-state RET rates for CO (as well as their scaling relations) have been studied by other investigators in the context of line broadening and mixing, and rates given by these scaling laws can be employed straightforwardly and confidently for a detailed analysis. For a particular laser pulse, we account for the laser transition by using the known Einstein B coefficient and the time-dependent laser intensity. For 2.35-μm excitation of CO, state-to-state RET rates were modeled with use of a modified exponential gap (MEG) scaling law similar to one used for studies of CO Raman line mixing.[19,20] The MEG scaling was chosen because it is straightforward to implement and it successfully reproduces line broadening and mixing in CO. In the form of MEG that is implemented here, endother-

mic RET rates were fit for collision-induced rotational state changes,

$$\mathrm{CO}(i) + \mathrm{M} \xrightarrow{k_{j\leftarrow i}} \mathrm{CO}(j) + \mathrm{M}, \tag{2}$$

through the use of the equation

$$k_{j\leftarrow i} = A\left(\frac{296}{T}\right)^{n}\left(\frac{1 + E_i/k_BT\delta}{1 + E_i/k_BT}\right)^{2}\exp(-\beta\Delta E/k_BT). \tag{3}$$

.

Here $k_{j\leftarrow i}$ is the transition rate from rotational state i to j; E_i is the energy of state i [J]; T is temperature [K]; $\Delta E \equiv E_j - E_i$, k_B is Boltzmann's constant [J/K]; and A [s^{-1}], β, δ, and n are fitting parameters. Exothermic reaction rates follow from detailed balance.

MEG parameters are fit for a particular bath gas so that the summed state transfer rates match measured or calculated FWHM line-broadening values from[20–23]

$$\pi c\Delta v_{c_i} \equiv \sum_{\substack{j=1\\ j\neq i}}^{\infty} k_{j\leftarrow i}. \tag{4}$$

Elastic dephasing and resonant rotation-rotation transfer can be ignored, since both pathways have been shown to have negligible effect on CO line mixing and broadening.[19,24] Rotational transfer rates in $v = 2$ are assumed to be identical to those in $v = 0$, since CO IR and Raman linewidths are constant with vibrational level.[20,24,25]

Given state-to-state RET rates, a spatial and temporal integration of state populations during pulsed excitation may be used to predict the dependence of LIF signal magnitude on fluence. We evaluated the predictions experimentally by measuring single-point LIF intensity as a function of pulse energy and comparing the intensity with the model predictions. A 250-mm focal length CaF_2 spherical lens was used to focus the 2.35-μm beam down to an approximately Gaussian waist with FWHM of 330 μm and a Rayleigh range of 43 mm. By focusing to a single point, we can achieve fluences approximately 300 times higher than those typically used in imaging experiments; high fluences lead to strongly non-Boltzmann distributions and allow for thorough evaluation of the quality of the RET model. The temporal profile of the near-IR (731 nm) OPO output was measured with a fast photodiode (Thorlabs DET-210), and the result after instrument function deconvolution (~6 ns FWHM Gaussian) was used as the temporal profile of the 2.35-μm pulse for the purposes of the calculations.

Calculations with the MEG scaling law (parameters for this mixture are $A = 2.0 \times 10^9\ s^{-1}$, $\beta = 1.3$, $\delta = 1.2$, and $n = 0.7$) are compared in Fig. 3 with the experimental data. The good agreement between the experiment and the MEG scaling-law model indicates that the MEG scaling-law analysis is quantitatively accurate and can be used to predict absorption processes.

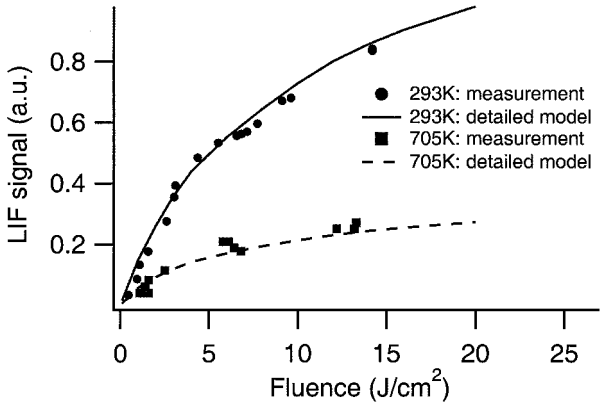

Fig. 3. Comparison of computational results and experimental measurements of LIF as a function of characteristic fluence, defined as pulse energy divided by square of beam waist FWHM. Measured LIF signal is relative. 293 K [$R(8)$ excitation] and 705 K [$R(12)$ excitation] experimental values are all scaled by a single constant factor, which is chosen to best match the computation.

Having matched the modeled RET rates to transition linewidths and having confirmed that the rate-equation analysis accurately predicts the growth of signal intensity with increasing fluence, we can use the MEG scaling-law calculations to confirm that typical experimental IR PLIF imaging experiments lead to linear fluorescence. The acceptable fluence is defined here as the maximum fluence for which the predicted errors in LIF signal that are caused by laser perturbation of state populations are below 10%; acceptable fluences are plotted as a function of temperature in Fig. 4 for a typical set of experimental parameters. The acceptable fluence range decreases with temperature, owing to decreased collision rates and smaller RET cross sections. For comparison, a typical value for laser fluence during planar excitation is shown, indicating that current

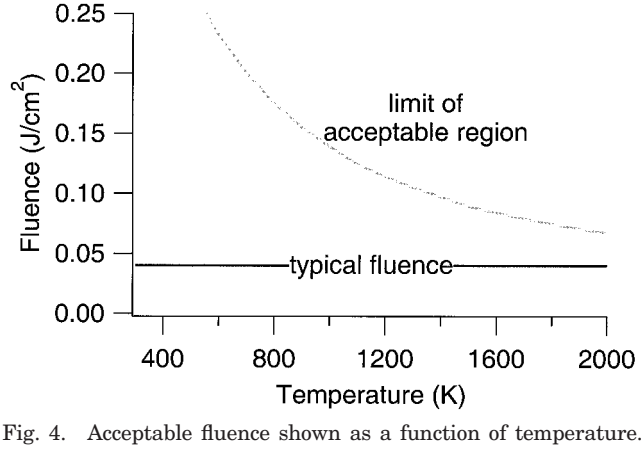

Fig. 4. Acceptable fluence shown as a function of temperature. Assumed experimental parameters are 1 atm, trace CO in air, the excitation of the strongest R line, a factor of two spatial variation of irradiance across the image owing to laser sheet profile nonuniformity and beam focusing, and 500-μm sheet thickness.

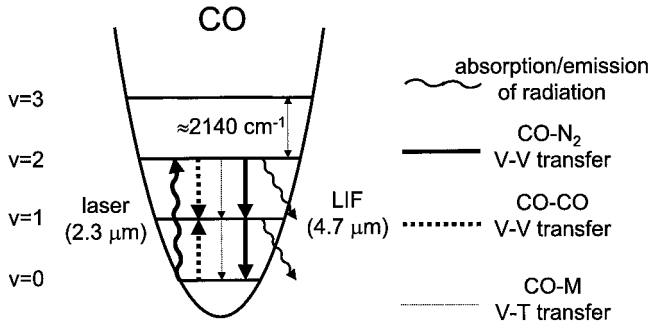

Fig. 5. CO excitation and collection scheme.

experiments are within the linear regime as defined above. Thus the perturbations of the state distribution are not large enough to affect the interpretation of IR PLIF signal.

2. Fluorescence

Having used RET calculations to confirm that typical fluences in IR PLIF experiments generate fluorescence within the linear regime, we use VET calculations to evaluate the effective fluorescence quantum yield ϕ. As described earlier, the goal of the excitation and collection scheme design is to make the value of $\sigma\phi$ uniform throughout the image.

In contrast to electronic PLIF measurements, for which the excited-state population typically can be modeled with good accuracy by an exponential decay with a single characteristic decay rate, the decay of the laser-induced vibrational nonequilibrium is not always exponential and can be dictated by several different types of energy-transfer processes. Selected VET processes for the CO excitation scheme are shown schematically in Fig. 5. Depending on the rates of these processes and the camera exposure time, the fluorescence quantum yield ϕ for IR PLIF measurements will not always take on a form similar to that used for electronic PLIF measurements. To describe the functional form expected for IR PLIF fluorescence quantum yield, we will discuss in this section the behavior of two systems: (1) a model four-level system that is greatly simplified and thereby helps to clarify the limiting behavior of IR PLIF schemes and (2) a fully resolved vibrational system whose modeling requires numerical integration but that accurately represents the vibrational manifolds of PLIF species and their collisional partners in combustion systems.

For the purposes of generating a qualitative understanding of how ϕ depends on VET rates, results are first presented for a model four-level system (Fig. 6). This model system treats molecular species as two-level systems and considers two diatomic species:

the LIF species L (the species that is excited by the laser and whose fluorescence is collected by the camera) and a near-resonant bath species B (a species that does not interact with the laser but has excited vibrational levels that are near-resonant with the excited levels of the LIF species). In treating species as two-level diatomic systems, this model system eliminates intramodal vibration-to-vibration (V-V) relaxation (which would be present if more than two levels were considered) and intermodal V-V relaxation (which would be present if polyatomics were considered). For LIF measurements in a pure gas, levels 3 and 4 are not used, and the system is effectively two-level.

Following laser excitation that populates level 2, the system equilibrates with other species through V-V processes at a characteristic rate denoted as k_{VV} and equilibrates with the translational temperature through vibration-to-translation (V-T) processes at a characteristic rate denoted as k_{VT}. V-T transfer proceeds by the following mechanisms:

$$\mathrm{L}(2) + \mathrm{M} \leftrightarrow \mathrm{L}(1) + \mathrm{M} + \Delta E_1, \tag{5}$$

with forward rate $N_2 k_{VT}$ and backward rate $N_1 k_{VT} \exp(-\Delta E_1/k_B T)$, and

$$\mathrm{B}(3) + \mathrm{M} \leftrightarrow \mathrm{B}(4) + \mathrm{M} + \Delta E_1 + \Delta E_2, \tag{6}$$

with forward rate $N_3 k_{VT}$ and backward rate $N_4 k_{VT} \exp[-(\Delta E_1 + \Delta E_2)/k_B T]$. V-V transfer proceeds by

$$\mathrm{L}(1) + \mathrm{B}(3) \leftrightarrow \mathrm{L}(2) + \mathrm{B}(4) + \Delta E_2. \tag{7}$$

with forward rate $N_1 N_3/N k_{VV}$ and backward rate $N_2 N_4/N k_{VV} \exp(-\Delta E_2)/k_B T)$. In all cases, M implies any molecule and N is the total population. The rate equations for this system are

$$\begin{aligned}
dN_1/dt &= N_2 k_{VT} - N_1 k_{VT} \exp(-\Delta E_1/k_B T) \\
&\quad - \frac{N_1 N_3}{N} k_{VV} + \frac{N_2 N_4}{N} k_{VV} \exp(-\Delta E_2/k_B T), \\
dN_2/dt &= N_2 k_{VT} - N_1 k_{VT} \exp(-\Delta E_1/k_B T) \\
&\quad + \frac{N_1 N_3}{N} k_{VV} - \frac{N_2 N_4}{N} k_{VV} \exp(-\Delta E_2/k_B T), \\
dN_3/dt &= N_4 k_{VT} - N_3 k_{VT} \exp[-(\Delta E_1 + \Delta E_2)/k_B T] \\
&\quad - \frac{N_1 N_3}{N} k_{VV} + \frac{N_2 N_4}{N} k_{VV} \exp(-\Delta E_2/k_B T), \\
dN_4/dt &= N_4 k_{VT} - N_3 k_{VT} \exp[-(\Delta E_1 + \Delta E_2)/k_B T] \\
&\quad + \frac{N_1 N_3}{N} k_{VV} - \frac{N_2 N_4}{N} k_{VV} \exp(-\Delta E_2/k_B T),
\end{aligned} \tag{8}$$

Although the major simplifications associated with the model four-level system prevent it from matching the exact behavior of a complete vibrational relaxation system, the model system's simplicity facilitates straightforward discussion of ϕ and its approximate dependence on experimental and physical parameters.

The fluorescence quantum yield ϕ is defined as the

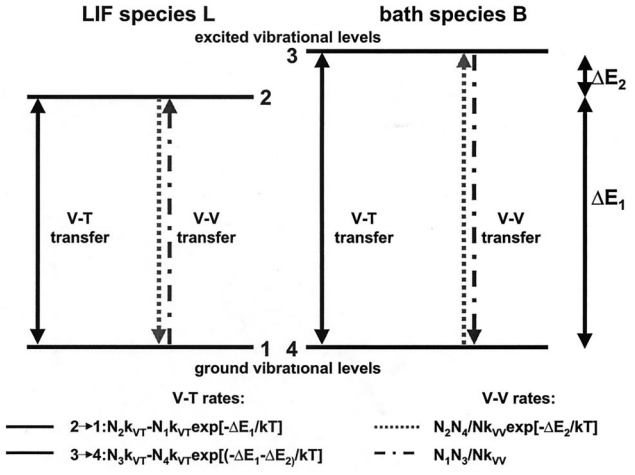

Fig. 6. VET rates for a model four-level system. Radiative transfer is a minor energy-transfer mechanism and is omitted from this figure.

number of emitted photons that are normalized by the number of absorbed photons $N_{p,\mathrm{abs}}$,

$$\phi = \sum_j \int_0^\tau \frac{\Delta N_j(t)}{N_{p,\mathrm{abs}}} A_j \mathrm{d}t\,, \tag{9}$$

where τ is the camera exposure time, $\Delta N_j(t)$ is the laser-induced population change in-state j, and A_j is the emission rate. Equation (9) reduces to simpler expressions in certain limits when the model four-level system from Fig. 6 is analyzed. Assuming, for simplicity, that the excited state is unpopulated before laser pumping, Eq. (9) becomes

$$\phi = \int_0^\tau A \frac{N_2(t)}{N_{p,\mathrm{abs}}}\,\mathrm{d}t. \tag{10}$$

Here $N_{p,\mathrm{abs}} = N_2(t = 0)$ is the number of absorbed photons or, equivalently, the number of molecules excited by the laser. Equation (10) simplifies further in certain limits, several of which are discussed in the following paragraphs.

Fast equilibration of pumped mode with translational mode. When the collisional V-T decay is fast compared to the camera exposure time and V-V equilibration is not present, the fluorescence quantum yield simplifies to a ratio of emission and collisional transfer rates. For example, the collisional decay time $1/k_{\mathrm{VT}}$ of CO_2 vibrational levels in 1 atm of H_2O is ~10 ns, and our minimum camera exposure times are 300 ns. For this case, $\tau \to \infty$, and Eq. (10) simplifies to the familiar ratio of emission and collision rates,

$$\phi = \int_0^\infty A \exp(-k_{\mathrm{VT}}t)\mathrm{d}t = A/k_{\mathrm{VT}}. \tag{11}$$

Short exposure time. When the camera exposure time is much shorter than the characteristic time of vibrational equilibration, vibrational level populations do not change during the exposure time, and the fluorescence quantum yield is simply the product of the emission rate and the exposure time. For example, IR PLIF of room-temperature CO might employ an integration time of ~0.5–10 μs, while the V-T energy transfer, which depletes the vibrational energy, occurs on millisecond time scales. In this case, $k_{\mathrm{VT}} \leftarrow 0$, and Eq. (10) simplifies to

$$\phi = \int_0^\tau A \exp(-k_{\mathrm{VT}}t)\mathrm{d}t = \int_0^\tau A\mathrm{d}t = A\tau. \tag{12}$$

Fast intermolecular vibrational equilibration, slow translational equilibration. When the system exchanges vibrational energy between molecules quickly but loses vibrational energy to the translational and rotational modes slowly, the V-V transfer is quickly equilibrated, and the V-T transfer is frozen. In this case, $k_{\mathrm{VT}} \to 0$ and $k_{\mathrm{VV}} \to \infty$. Thus only k_{VV} terms in Eqs. 8 are retained, and the equilibrium between levels 2 and 3 is described by detailed balance:

$$\frac{N_1 N_3}{N} = \frac{N_2 N_4}{N} \exp(-\Delta E_2/kT). \tag{13}$$

The vibrational energy, which was initially held by the LIF molecules in level 2, is now shared between LIF and bath species in proportion to their mole fractions:

$$\frac{N_2}{\chi_L} = \frac{N_3}{\chi_B} \exp(\Delta E_2/k_B T), \tag{14}$$

Here it is assumed that the vibrational excitation is small, therefore $N_1/N \approx \chi_L$ and $N_4/N \approx \chi_B$, where χ_L is the mole fraction of the LIF species L and χ_B is the mole fraction of the bath gas species B. Noting that, for $k_{\mathrm{VT}} \to 0$, $N_2 + N_3 = N_{p,\mathrm{abs}}$, and substituting Eq. (14) into Eq. (10), we can show that the vibrational energy in the fluorescing molecule is diluted by the bath gas, attenuating the PLIF signal:

$$\phi = A\tau \frac{\chi_L}{\chi_L + \chi_B \exp(-\Delta E_2/k_B T)}. \tag{15}$$

For large ΔE_2, Eq. (15) becomes Eq. (12), while for small ΔE_2, this simplifies to

$$\phi = A\tau \frac{\chi_L}{\chi_L + \chi_B}. \tag{15}$$

While the above results apply rigorously only to the model four-level system and thus give only semiquantitative results for real systems, they serve to identify which parameters will be important for PLIF signal and which excitation schemes will be most successful. IR PLIF signal is most easily interpreted if the limit in Eq. (12) is reached, since signals are independent of collisional environment. In cases with rapid resonant V-V transfer (CO_2 in N_2), fluorescence quantum yield may scale approximately with mole fraction, as described by Eq. (16). The form in Eq.

Table 1. Sample References Providing VET Data for Use in Calculating Fluorescence Quantum Yield

VET Process	References
CO+M V-T	28–32
N_2+M V-T	28, 33
O_2+M V-T	28, 34
H_2O+M V-T	35, 36
CO-CO V-V	32, 37
CO-N_2 V-V	29, 38, 39
CO-H_2O V-V	40, 41
CO-CO_2 V-V	16, 42–47
CO-O_2 V-V	30
CO_2-M V-T and V-V	17, 18, 36, 43, 45, 48–55
CO_2CO_2 V-V	17
CO_2-N_2 V-V	43, 44
N_2-N_2 V-V	33
O_2-O_2 V-V	34

(16) generates higher image contrast, since the fluorescence quantum yield increases the dependence of PLIF signal on the mole fraction or concentration of the imaged species, but makes a quantitative interpretation more challenging. In all cases, the presence of a rapid V-T quencher (e.g., H_2O for IR PLIF of CO_2) can lead to PLIF signals that are inversely proportional to VET rates [Eq. (11)]. As is discussed in the following sections, straightforward interpretation of PLIF signal in the linear regime can easily be achieved for CO but is more challenging for CO_2; the presence of fast VET transfer for CO_2 will motivate consideration of laser-saturated schemes for excitation.[14]

The limits described in Eqs. (11)–(15) are useful conceptual guidelines but are only approximate; ϕ can be quantitatively evaluated only through the integration of Eq. (9). Starting with an initial condition that assumes a laser-induced vibrational nonequilibrium, our detailed VET model uses a rate-equation formulation and the CHEMKIN interface[26] to solve for the vibrational level populations as a function of time. The model assumes translational and rotational equilibrium (i.e., a common rotational and translational temperature), since these modes equilibrate very quickly as compared with the camera integration time. The CHEMKIN interface and solver is adapted for VET through (1) modification of the thermodynamic database to treat vibrational levels as individual species, (2) the fitting of curves to experimental or computational transfer rate data from a variety of references, and (3) the use of Schwartz-Slawsky-Herzfeld theory[27] to scale experimental and calculated rates for low-lying vibrational levels for use at higher levels. Table 1 lists a number of VET references used, and key energy-transfer rates for CO and CO_2 in a typical fuel-rich hydrocarbon flame gas mixture are shown in Fig. 7. The CHEMKIN interface provides reverse reaction rates consistent with detailed balance. Roughly 80 vibrational levels and 14,000 energy-transfer processes are used.

The detailed VET model has been used to compute

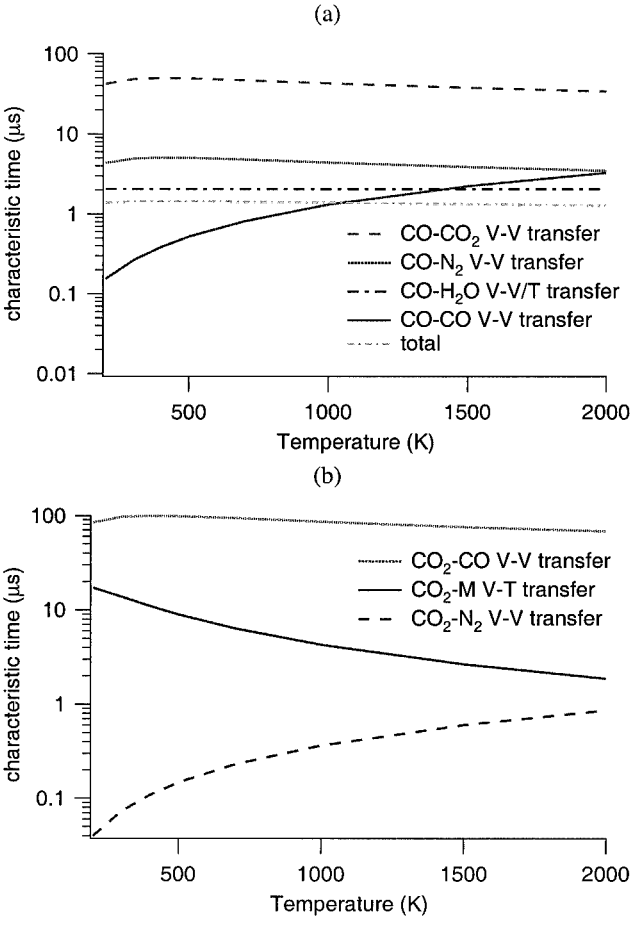

Fig. 7. Characteristic times for VET as a function of temperature and collision partner at 1 atm. (a) Rates for CO in a mixture of 5% CO, 10% CO_2, and 10% H_2O in N_2. O_2 and inert gases are inefficient VET partners and are not considered. (b) Rates for CO_2 in the same mixture. Temperature dependences are stronger for CO_2 than CO owing to the nonresonant nature of the intermodal V-V transfer.

ϕ for CO following 2ν excitation. Figure 8 shows results as a function of temperature, camera exposure time, strength of excitation, CO mole fraction, and H_2O mole fraction [approximate prediction of Eq. (12); $\phi = 7 \times 10^{-5}$ for a 1-μs exposure]. For short exposures, the system approaches the no-quench limit of Eq. (12), while for longer exposures, the effects of energy-transfer processes are evident [Fig. 8(a)]. Exposure times near 1 μs are a good compromise between the minimization of ϕ variations and the maximization of signal levels, and exposures near 1 μs are typically used for flame experiments. Strength of excitation (defined here as the fraction of molecules in the lower vibrational level that are pumped to the upper level) does not affect ϕ for CO, since translational heating during the exposure time is negligible [Fig. 8(b)]. The fluorescence quantum yield ϕ shows minor dependence on CO mole fraction at high temperatures [Fig. 8(c)]. In this case, increased CO mole fraction minimizes the effects of vibrational energy dilution by resonant bath gases

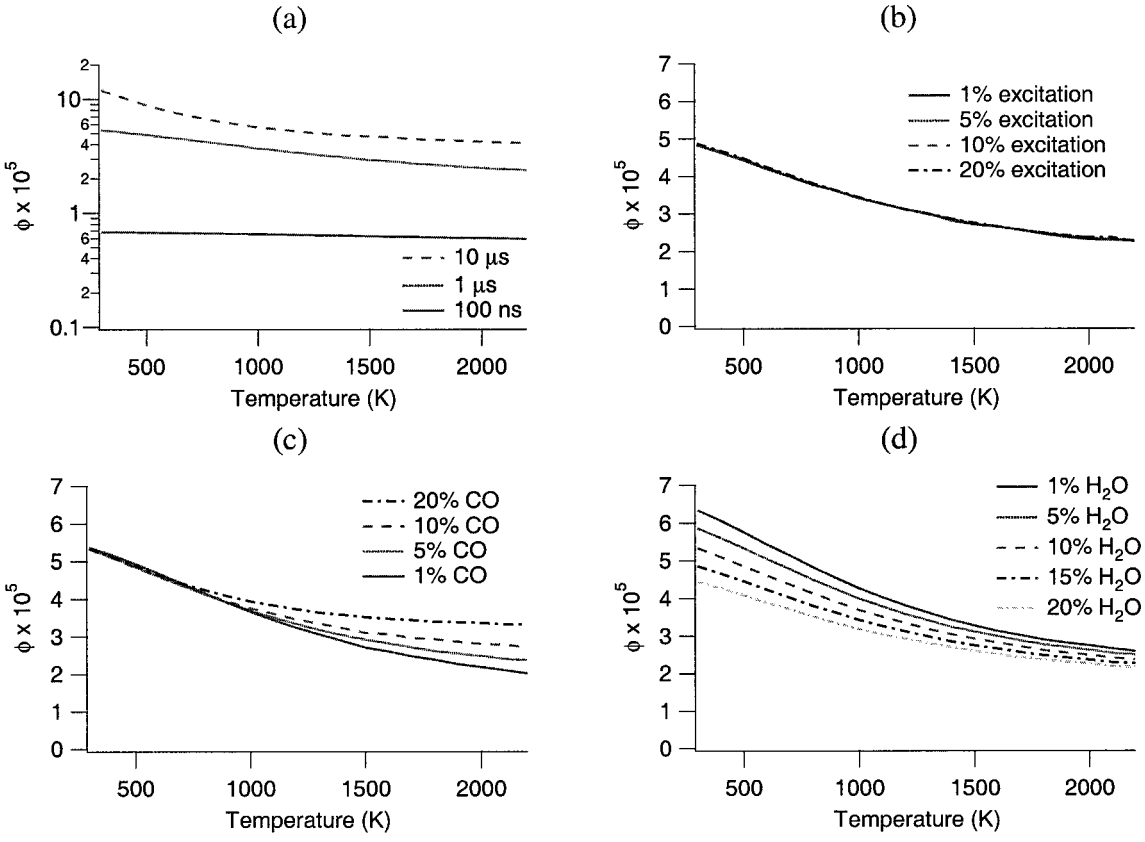

Fig. 8. Effects of (a) exposure time, (b) strength of excitation, (c) CO mole fraction, and (d) H_2O mole fraction on ϕ for CO. Nominal parameters are 1-μs exposure; 10% excitation; and mixture constituents 5% CO, 15% H_2O, 15% CO_2 in N_2. In each graph, one parameter is varied from the nominal value, while other values are held constant.

(CO_2, N_2), as expressed in Eq. (15). These dilution effects become more prominent as temperature increases, since the increased translational energy decreases the effect of the energy gap associated with transfer from CO to N_2 and CO_2 (about 200 cm^{-1} or 300 K energy defect). At the CO levels that are observed in most hydrocarbon flames (<5%), the maximum variation of ϕ with CO mole fraction for a 1 μs exposure is ±7%. Note that this variation is much less than that predicted by Eq. (15), which sets an upper bound for these effects. H_2O accelerates translational equilibration at all temperatures, and for a 1-μs exposure ϕ varies by ±15% as water mole fraction is varied 0–20% [Fig. 8(d)]. In both cases, variations are significantly smaller for 1-μs exposures than they are in the long-exposure limit [Eq. (11)].

The above results show that the effects of varying bath gas composition are manageable, and that a single curve [Fig. 8(b)] describes the dependence of ϕ with temperature with use of an appropriate exposure time. With this in mind, we may choose excitation of specific rotational lines to minimize the variation of signal levels for a particular temperature range. With the appropriate excitation line, PLIF signal levels are directly proportional to species concentration. Figure 9 shows the product of the fluorescence quantum yield ϕ and the absorption cross section σ. By choosing a particular rotational line, $\phi\sigma$, and therefore PLIF signal per CO molecule, can be made approximately independent of temperature within certain temperature ranges. Specifically, the $R(24)$ line generates signal that is constant to within

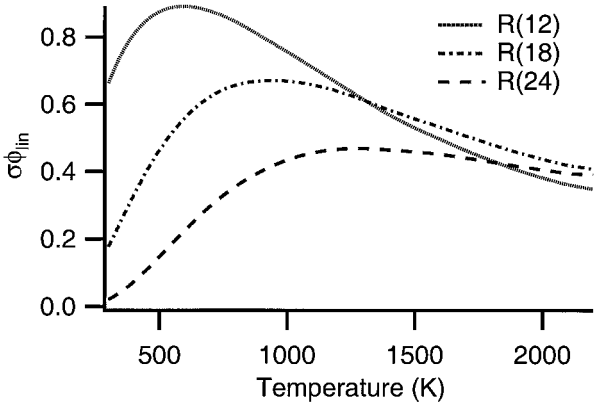

Fig. 9. Product of absorption cross section and fluorescence quantum yield for CO [normalized to $R(7)$ line at 300 K] as a function of pumped line and temperature at 1 atm. The gas mixture is the same as was used for Fig. 8. Spectrally narrow laser excitation at the line center is assumed. From this graph, lines may be chosen that have roughly constant $\sigma\phi$ (±15%) in various regions ranging from room temperature to 2200 K.

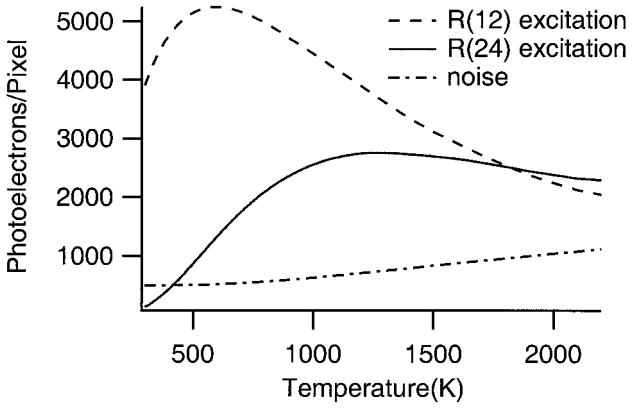

Fig. 10. Calculated fluorescence signal as compared with noise levels for the IR PLIF of CO. $n_{CO} = 1.7 \times 10^{17}$ cm^{-3}, corresponding to 5% CO at 2200 K and 1 atm. Bath gas is 15% H_2O and 15% CO_2, with a balance of N_2. Other parameters are 1-μs exposure, 10-mJ excitation pulse, and 8 cm × 8 cm image.

±12% over the 800–2200 K range, and the $R(12)$ line generates signal that is constant to within ±15% over the 300–800 K range.

3. Sensitivity

The predicted sensitivity of IR PLIF techniques is evaluated by comparing signal levels with noise that comes from analog-to-digital conversion (read noise) and background subtraction (shot noise). Read noise for the camera systems is approximately 500 photoelectrons per pixel. Shot noise from background subtraction is a function of the experiment; typical values can be as high as 1000 photoelectrons at high temperatures if spectrally wide filters are used or if soot is present. Figure 10 plots signal levels for two excitation lines as a function of temperature at conditions given in the figure caption. Note that signal is higher than the noise for both excitation lines for these conditions. This plot shows that the single-shot imaging of nascent levels of CO is possible with use of IR PLIF.

B. CO_2 Excitation Schemes

CO_2 is much more complicated to notate and model than CO, owing to its multiple vibrational modes, Fermi resonance, and faster VET processes. Carbon dioxide level notation analogous to that of HITRAN[56,57] is used here as well as compact notation to describe these groups of vibrational levels as units. This compact notation uses a level symbol with unspecified axial spin momentum (e.g., 110) to indicate the group of levels corresponding to that energy (in this case, 11^00_I, 11^00_{II}, and 03^30).

Several excitation options are available for CO_2, including combination bands at 2.0 μm ($20^01_{II} \leftarrow 00^00$) and 2.7 μm ($10^01_{II} \leftarrow 00^00$) and difference bands at 9.6 μm ($00^01 \leftarrow 10^00_{II}$) and 10.6 μm ($00^01 \leftarrow 10^00_I$). In all cases, fluorescence is collected through the fundamental band at 4.3 μm. For hydrocarbon flames, absorption interferences at the laser wavelength are minor at 9.6, 10.6, and 2.0 μm; excitation at 2.7 μm, though, poses some experimental challenges, as laser attenuation that is due to ambient water and CO_2 must be eliminated through the purge of CO_2 and H_2O from the beam path between the laser and the imaged plane. Experiments to date using our OPO source (see Fig. 1) have employed 2.0-μm excitation. A separate paper[14] discusses 10.6-μm excitation with use of a CO_2 laser.

1. Absorption

RET analysis similar to that for CO is used to evaluate acceptable fluences for CO_2 excitation schemes. VET must be considered for CO_2, since vibrational transfer rates between near-resonant states in CO_2 can be within 1 order of magnitude of rotational transfer rates. For 2.0-μm excitation, the pertinent energy-transfer processes are (a) collisional RET in the lower (00^00) and upper (20^01_{II}) vibrational levels of the laser transition and (b) VET between the nine vibrational levels in the 201 manifold. Analysis of 2.7, 9.6, and 10.6-μm excitation schemes are analogous except for differences in lower and upper vibrational level degeneracies. State-to-state RET rates were used only in the vibrational levels connected by the laser transition; other vibrational levels were assumed to be in rotational equilibrium.

A simple MEG scaling is used for CO_2 as well, even though more physically accurate energy-corrected sudden models[55,58–60] have been proposed. This is justified since the laser transitions in $^{12}C^{16}O_2$ are between levels with axial spin momentum Σ^+; for these levels, nonzero rotational populations occur in only half of the rotational states, and propensity differences between even-Δj and odd-Δj transitions (which stem from angular-momentum couplings and are absent from MEG scalings) are unimportant. For a particular choice of bath gas, fitting parameters are calculated so as to best match the linewidths for rotational states up to $j = 100$, as calculated using the results of.[61] Previous work has confirmed the accuracy of the linewidth-fitting technique,[62–65] as well as the validity of using one set of RET rates for all vibrational levels.[66,67]

For transitions between the degenerate or near-degenerate levels in the 201, 101, or 100 manifolds, experimental rates[55] are used, with quantum state scaling from Schwartz-Slawsky-Herzfeld theory[27] and temperature dependence chosen to match that of the $10^00_I \leftrightarrow 10^00_{II}$ transition as calculated inRef. 50.

This energy-transfer analysis leads to acceptable fluence limits (<10% error), which are listed in Table 2 for a typical set of experimental parameters. For CO_2, 2.0-μm excitation clearly allows for excitation in the linear regime (since of the bands listed its absorption is weakest), while excitations at 2.7, 9.6, or 10.6 μm experience significant departure from linearity and are more appropriate for saturated excitation techniques.[14]

2. Fluorescence

For CO_2, fluorescence is collected at 4.3 μm, corresponding to single-quantum changes in asymmetric

Table 2. Acceptable Fluence (<10% Error in LIF Signal) Shown for Several CO_2 Excitation Schemes at 1500 K[a]

Excitation Scheme	Acceptable Fluence[b]
2.0 μm	1.160
2.7 μm	0.015
9.6 μm	0.025
10.6 μm	0.031
typical experimental fluence	0.040

[a]A typical fluence level used in experiments is listed for comparison. Assumed experimental parameters are the same as for Fig. 4.
[b]In J/cm^2.

stretch (ν_3) energy. The laser-induced excess of ν_3 energy is depleted by nonresonant intermodal V-V transfer (upon collisions with any molecule M) and by near-resonant transfer (upon collisions with CO and N_2). Because nonresonant transfer plays an important role in the vibrational relaxation of CO_2, H_2O's enhanced V-T transfer rates strongly affect CO_2 vibrational relaxation.[35] Also, because the characteristic time for CO_2–N_2 V-V transfer is on the order of 100 ns,[50] N_2 dilutes CO_2 LIF signal [Eq. (16)]. Unfortunately, these two effects cause CO_2 fluorescence quantum yield to vary widely on the basis of the collisional environment (Fig. 11). From this figure, it is clear that the uniformity of fluorescence quantum yield that was possible for CO cannot be readily achieved for CO_2.

The variations in ϕ caused by N_2 and H_2O mole fraction variations are compounded by the thermal dependence of the absorption cross section of CO_2 (Fig. 12), which is much more significant than that of CO owing to CO_2's rapidly changing vibrational partition function, which is typical of triatomics. Taken together, collider-dependent fluorescence quantum yield and temperature-dependent absorption cross section make the nanosecond-pulse excitation of CO_2 in the linear regime suitable only for qualitative visualization. While these challenges limit the potential utility of linear IR PLIF imaging techniques for

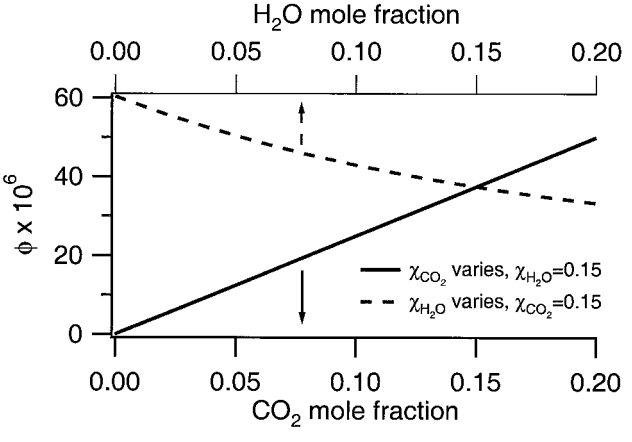

Fig. 11. Predicted CO_2 fluorescence quantum yield ϕ for linear excitation and 1-μs exposure. Nominal gas mixture is 15% H_2O and 15% CO_2, with a balance of N_2, at 1000 K. Curves show effect as mole fraction of CO_2 or H_2O is changed.

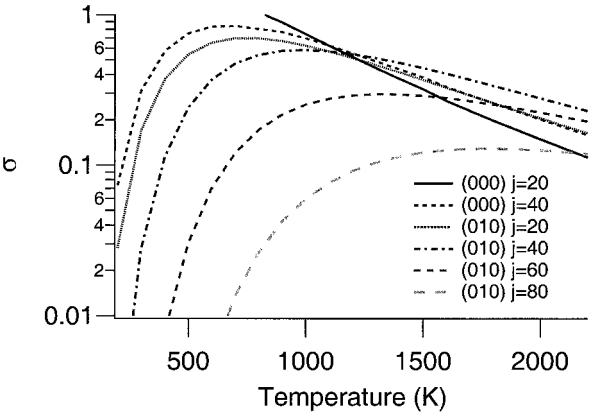

Fig. 12. CO_2 absorption cross section [normalized to $R(30)$ line at 300 K] as a function of pumped line and temperature (for R transitions). Legend indicates the lower vibrational level (00^00 or 01^10) and rotational state. Spectrally narrow laser excitation is assumed.

CO_2, they may be overcome with use of laser-saturated techniques,[14] which have the potential to simplify greatly interpretation of CO_2 IR PLIF images.

4. Conclusions

Linear excitation schemes for IR PLIF imaging of CO and CO_2 have been presented. A model four-level system is analyzed to describe the limiting behavior or the fluorescence quantum yield, highlighting differences in IR LIF dependence on the basis of the relative length of time scales for camera exposure, V-T transfer, and V-V transfer. Integration of vibrational level populations in a fully resolved vibrational manifold is used to quantify fluorescence quantum yield and its dependence on bath gas temperature and species constituents in the general case.

For CO, excitation at 2.35 μm followed by a 1-μs camera integration at 4.7 μm generates high signal levels while minimizing laser scattering, laser attenuation, radiative trapping, and fluorescence quantum yield variations. For CO, the VET is slow enough that microsecond-scale integration times provided by our IR camera system effectively freeze the vibrational populations and make the fluorescence quantum yield approximately independent of the collisional environment. The $R(12)$ and $R(24)$ lines may then be used to generate nearly temperature-independent signal within the 300–800 K and 800–2200 K regions, respectively.

A detailed rate-equation analysis of the transient absorption process in the presence of RET shows that typical experimental fluences reside within the linear regime and standard PLIF postprocessing techniques may be used. A detailed MEG scaling-law analysis properly predicts LIF signal over the wide range of fluences possible for single-point measurements and planar imaging. Calculations of signal and noise levels indicate that IR PLIF is sensitive enough to enable single-shot imaging of nascent CO in flames.

For CO_2, 2.0-μm excitation (followed by collection

at 4.3 μm) is the best option for linear fluorescence measurements, as it avoids laser attenuation from CO_2 and H_2O (which is observed at 2.7 μm) and nonlinear absorption (which is predicted for typical experimental fluences at 2.7, 9.6, and 10.6 μm). The quantitative accuracy of CO_2 images is limited by CO_2's rapidly varying partition function and the effects of H_2O and N_2 mole fractions on fluorescence quantum yield. These challenges may be circumvented through high-pulse-energy excitation and saturated fluorescence, which is considered in a separate paper.[14]

Future work to extend these measurements to CH_4 appears quite feasible. In the conditions in which CH_4 is used as a fuel, its ν_4 vibrational mode experiences slow V-T relaxation times (~1 μs). CH_4 may be excited at 2.3 or 3.3 μm, and ν_4 emission at 7.6 μm is expected to generate large signals. This emission, though, must be probed using short-gate long-wave infrared cameras, which are not presently available.

This research was supported by the Air Force Office of Scientific Research, Aerospace and Materials Sciences Directorate, with Julian Tishkoff as technical monitor.

References

1. B. J. Kirby and R. K. Hanson, "Planar laser-induced fluorescence imaging of carbon monoxide using vibrational (infrared) transitions," Appl. Phys. B **69,** 505–507 (1999).
2. B. J. Kirby and R. K. Hanson, "Imaging of CO and CO_2 using infrared planar laser-induced fluorescence," Proc. Combust. Inst. **28,** 253–259 (2000).
3. J. M. Seitzman and R. K. Hanson, "Planar fluorescence imaging in gases," in *Experimental Methods for Flows with Combustion*, A. Taylor, ed. (Academic, London, 1993).
4. M. B. Long, D. C. Fourguette, and M. C. Escoda, "Instantaneous Ramanography of a turbulent diffusion flame," Opt. Lett. **8,** 244–246 (1983).
5. J. M. Seitzman, J. Haumann, and R. K. Hanson, "Quantitative two-photon LIF imaging of carbon monoxide in combustion gases," Appl. Opt. **26,** 2892–2899 (1987).
6. N. Georgiev and M. Aldén, "Two-dimensional imaging of flame species using two-photon laser-induced fluorescence," Appl. Spectrosc. **51,** 1229–1237 (1997).
7. G. Juhlin, H. Neij, M. Versluis, B. Johansson, and M. Alden, "Planar laser-induced fluorescence of H_2O to study the influence of residual gases on cycle-to-cycle variations in SI engines," Combust. Sci. Technol. **132,** 75–97 (1998).
8. W. P. Partridge, J. R. Reisel, and N. M. Laurendeau, "Laser-saturated fluorescence measurements of nitric-oxide in an inverse diffusion flame," Combust. Flame **116,** 282–290 (1999).
9. M. Alden, P. Grafstrom, H. Lundberg, and S. Svanberg, "Spatially resolved temperature measurements in a flame using laser-excited two-line atomic fluorescence and diode array detection," Opt. Lett. **8,** 241–243 (1983).
10. B. Hiller and R. K. Hanson, "Simultaneous planar measurements of velocity and pressure fields in gas flows using laser-induced fluorescence," Appl. Opt. **27,** 33–48 (1988).
11. J. Rehm and P. H. Paul, "Reaction rate imaging," Proc. Combust. Inst. **28,** 1775–1782 (2000).
12. K. Kohse-Hoinghaus, "Laser techniques for the quantitative detection of reactive intermediates in combustion systems," Prog. Energy Combust. Sci. **20,** 203–279 (1994).
13. M. Alden, "Laser spectroscopic techniques for combustion diagnostics," Combust. Sci. Technol. **149,** 1–18 (1999).
14. B. J. Kirby and R. K. Hanson, "CO_2 imaging using saturated planar laser-induced vibrational fluorescence," Appl. Opt. **20,** 6136–6144 (2001).
15. B. K. McMillin, J. L. Palmer, and R. K. Hanson, "Temporally resolved, two-line fluorescence imaging of NO temperature in a transverse jet in a supersonic crossflow," Appl. Opt. **32,** 7532–7545 (1993).
16. D. F. Starr and J. K. Hancock, "Vibrational energy transfer in CO_2-CO mixtures from 163 to 406°K," J. Chem. Phys. **63,** 4730–4734 (1975).
17. Jack Finzi and C. Bradley Moore, "Relaxation of $CO_2(10^01)$, $CO_2(02^01)$, and $N_2O(10^01)$ vibrational levels by near-resonant $V \rightarrow V$ energy transfer," J. Chem. Phys. **63,** 2285–2288 (1975).
18. L. Doyennette, M. Margottin-Maclou, A. Chakroun, H. Gueguen, and L. Henry, "Vibrational energy transfer from (00^01) level of $^{14}N_2O$ and $^{12}CO_2$ to $(m, n^l,1)$ levels of these molecules and of their isotopic species," J. Chem. Phys. **62,** 440–447 (1975).
19. J. P. Looney, G. J. Rosasco, L. A. Rahn, W. S. Hurst, and J. W. Hahn, "Comparison of rotational relaxation rate laws to characterize the Raman Q-branch spectrum of CO at 295 K," Chem. Phys. Lett. **161,** 232–238 (1989).
20. G. J. Rosasco, L. A. Rahn, W. S. Hurst, R. E. Palmer, and S. M. Dohne, "Measurement and prediction of Raman *Q*-branch line self-broadening coefficients for CO from 400 to 1500 K," J. Chem. Phys. **90,** 4059–4068 (1989).
21. T. Nakazawa and M. Tanaka, "Measurements of intensities and self- and foreign-gas-broadened half-widths of spectral lines in the CO fundamental band," J. Quant. Spectrosc. Radiat. Transfer **28,** 409–416 (1982).
22. J. M. Hartmann, L. Rosenmann, M. Y. Perrin, and J. Taine, "Accurate calculated tabulations of CO line broadening by H_2O, N_2, O_2, and CO_2 in the 200–3000-K temperature range," Appl. Opt. **27,** 3063–3065 (1988).
23. J-P. Bouanich, "Determination experimentale des largeurs et des deplacements des raies de la bande 0–2 de CO perturbe par les gas rares (He, Ne, Ar, Kr, Xe)," J. Quant. Spectrosc. Radiat. Transfer **12,** 1609–1615 (1972).
24. J. J. Belbruno, J. Gelfand, and H. Rabitz, "Collision dynamical information from pressure broadening measurements: application to carbon monoxide," J. Chem. Phys. **78,** 3990–3998 (1983).
25. P. L. Varghese and R. K. Hanson, "Room-temperature measurements of collision widths of CO lines broadened by H_2O," J. Mol. Spectrosc. **88,** 234–235 (1981).
26. R. J. Kee, F. M. Rupley, and J. A. Miller, "Chemkin-II: a Fortran chemical kinetics package for the analysis of gas phase chemical kinetics," Tech. Rep. SAND89–8009B, (Sandia National Laboratories, Livermore, Calif., 1992).
27. J. T. Yardley, "*Introduction to Molecular Energy Transfer* (Academic, New York, 1980).
28. R. C. Millikan and D. R. White, "Systematics of vibrational relaxation," J. Chem. Phys. **39,** 3209–3213 (1963).
29. D. F. Starr, J. K. Hancock, and W. H. Green, "Vibrational deactivation of carbon monoxide by hydrogen and nitrogen from 100 to 650 degrees K," J. Chem. Phys. **61,** 5421–5425 (1974).
30. T. C. Price, D. C. Allen, and C. J. S. M. Simpson, "Vibrational deactivation of CO (v=1) by O_2 measured between 300 and 80 K," Chem. Phys. Lett. **53,** 182–184 (1978).
31. D. C. Allen, T. J. Price, and C .J. S. M. Simpson, "Low-temperature vibrational-relaxation of carbon-monoxide by light mass species," Chem. Phys. **41,** 449–460 (1979).
32. M. Cacciatore and G. D. Billing, "Semiclassical calculation of VV and VT rate coefficients in CO," Chem. Phys. **58,** 395–407 (1981).
33. G. D. Billing and E. R. Fisher, "VV and VT-rate coefficients in

N_2 by a quantum-classical model," Chem. Phys. **43,** 395–401 (1979).
34. G. D. Billing and R. E. Kolesnick, "Vibrational relaxation of oxygen. State to state rate constants," Chem. Phys. Lett. **200,** 382–386 (1992).
35. R. T. V. Kung and R. E. Center, "High temperature vibrational relaxation of H_2O by H_2O, He, Ar, and N_2," J. Chem. Phys. **62,** 2187–2194 (1975).
36. D. C. Allen, T. J. Price, and C.J. S. M. Simpson, "Vibrational deactivation of the bending mode of CO_2 measured between 1500 K and 150 K," Chem. Phys. Lett. **45,** 183–187 (1977).
37. H. T. Powell, "Vibrational relaxation of carbon monoxide using a pulse discharge. II. T=100, 300, 500 K," J. Chem. Phys. **63,** 2635–2645 (1975).
38. G. D. Billing, "Vibration/vibration energy transfer in CO colliding with $^{14}N_2$, $^{14}N^{15}N$ and $15N_2$," Chem. Phys. **50,** 165–173 (1980).
39. M. Cacciatore, M. Capitelli, and G. D. Billing, "Theoretical semiclassical investigation of the vibrational relaxation of CO colliding with $14N_2$," Chem. Phys. **89,** 17–31 (1984).
40. J. C. Stephenson and E. R. Mosburg, "Vibrational energy transfer in CO from 100 to 300 °K," J. Chem. Phys. **60,** 3562–3566 (1974).
41. B. Wang, Y. Gu, and F. Kong, "Rapid vibrational quenching of CO(V) by H_2O and C_2H_2," J. Phys. Chem. A **103,** 7395–7400 (1999).
42. A. Chakroun, M. Margottin-Maclou, H. Gueguen, L. Doyennette, and L. Henry, "Vibrational deexcitation of carbon-dioxide and nitrous-oxide excited in (00^01) vibrational level and vibrational energy-transfer in CO_2-CO from 150 K to 300 K," Comptes Rendus Hebdomadaires Des Seances De L Academie Des Sciences Serie B, **281,** 29–32 (1975).
43. J. Taine, F. Lepoutre, and G. Louis, "Photoacoustic study of collisional deactivation of CO_2 by N_2, CO, and O_2 between 160 K and 375 K," Chem. Phys. Lett. **58,** 611–615 (1978).
44. J. Taine and F. Lepoutre, "Photoacoustic study of the collisional deactivation of the first vibrational levels of CO_2 by N_2 and CO," Chem. Phys. Lett. **65,** 554–558 (1979).
45. J. Taine and F. Lepoutre, "Determination of energy transferred to rotation: translation in deactivation of $CO_2(00^01)$ by N_2 and O_2 and of CO(1)by CO_2, " Chem. Phys. Lett. **75,** 448–451 (1980).
46. B. S. Wang, Y. S. Gu, and F. N. Kong, "Multilevel vibrational-vibrational (V-V) energy transfer from CO(v) to O_2 and CO_2," J. Phys. Chem. A **102,** 9367–9371 (1998).
47. G. E. Caledonia, B. D. Green, and R. E. Murphy, "Study of the vibrational level dependent quenching of CO(v = 1–16) by CO_2," J. Chem. Phys. **71,** 4369–4379 (1979).
48. F. Lepoutre, G. Louis, and J. Taine, "Photoacoustic study of intra-molecular energy transfer in CO_2 deactivated by monatomic gases between 153 K and 393 K," J. Chem. Phys. **70,** 2225–2235 (1979).
49. J. Taine and F. Lepoutre, "Temperature-dependence of the $CO_2(01^10)$ collisional deactivation rate constants between 170 K and 400 K, " Chem. Phys. Lett. **75,** 452–455 (1980).
50. G. D. Billing, "Semiclassical calculation of energy transfer in polyatomic molecules. VII. intra- and inter-molecular energy transfer in N_2 + CO_2," Chem. Phys. **67,** 35–47 (1982).
51. C. Dang, J. Reid, and B. K. Garside, "Detailed vibrational population distributions in a CO_2 laser discharge as measured with a tunable diode laser," Appl. Phys. B **27,** 145–151 (1982).
52. C. Dang, J. Reid, and B. K. Garside, "Dynamics of the CO_2 lower laser levels as measured with a tunable diode laser," Appl. Phys. B **31,** 163–172 (1983).
53. G. D. Billing, "Semiclassical calculation of energy transfer in polyatomic molecules. XI. cross sections and rate constants for Ar+CO_2," Chem. Phys. **91,** 327–339 (1984).
54. G. Jolicard and M. Y. Perrin, "Vibrational energy transfers in polyatomic molecules: a vibrational effective Hamiltonian approach for the CO_2-Ar system," Chem. Phys. **123,** 249–265 (1988).
55. G. Millot and C. Roche, "State-to-state vibrational and rotational energy transfer in CO_2 gas from time-resolved Raman-infrared double-resonance experiments," J. Raman Spectrosc. **29,** 313–320 (1998).
56. L. S. Rothman, C. P. Rinsland, A. Goldman, S. T. Massie, D. P. Edwards, J. M. Flaud, A. Perrin, C. Camy-Peyret, V. Dana, J. Y. Mandin, J. Schroeder, A. McCann, R. R. Gamache, R. B. Wattson, K. Yoshino, K. V. Chance, K. W. Jucks, L. R. Brown, V. Nemtchinov, and P. Varanasi, "The HITRAN molecular spectroscopic database and HAWKS (HITRAN atmospheric workstation): 1996 edition," J. Quant. Spectrosc. Radiat. Transfer **60,** 665–710 (1998).
57. L. S. Rothman and L. D. G. Young, "Infrared energy levels and intensities of carbon dioxide–II," J. Quant. Spectrosc.Radiat. Transfer **25,** 505–524 (1981).
58. R. Rodrigues, Gh. Blanquet, J. Walrand, B. Khalil, R. Le Doucen, F. Thibault, and J.-M. Hartmann, "Line-mixing effects in Q branches of CO_2. I: Influence of parity in $\Delta \leftrightarrow \Pi$ bands," J. Mol. Spectrosc. **186,** 256–268 (1997).
59. L. Bonamy, J. Bonamy, D. Robert, A. Deroussiaux, and B. Lavorel, "A direct study of the vibrational bending effect in line mixing: the hot degenerate $11^10 \leftarrow 01^10$ transition of CO_2, " J. Quant. Spectrosc. Radiat. Transfer **57,** 341–348 (1997).
60. N. N. Filippov, J.-P. Bouanich, J.-M. Hartmann, L. Ozanne, C. Boulet, M. V. Tonkov, F. Thibault, and R. Le Doucen, "Line-mixing effects in the $3\nu_3$ band of CO_2 perturbed by Ar," J. Quant. Spectrosc. Radiat. Transfer **55,** 307–320 (1996).
61. L. Rosenmann, J. M. Hartmann, M. Y. Perrin, and J. Taine, "Accurate calculated tabulations of IR and Raman CO_2 line broadening by CO_2, H_2O, N_2, O_2 in the 300–2400-K temperature range," Appl. Opt. **27,** 3902–3907 (1988).
62. M. Margottin-Maclou, F. Rachet, C. Boulet, A. Henry, and A. Valentin, "Q-branch line mixing effects in the $(20^00)_I \leftarrow 01^10$ and $(12^20)_I \leftarrow 01^10$ bands of carbon dioxide," J. Mol. Spectrosc. **172,** 1–15 (1995).
63. L. L. Strow and B. M. Gentry, "Rotational collisional narrowing in an infrared CO_2 Q-branch studied with a tunable-diode laser," J. Chem. Phys. **84,** 1149–1156 (1986).
64. T. Huet, N. Lacome, and A. Lévy, "Line mixing effects in the Q branch of the $10^0 \leftarrow 01^10$ transition of CO_2," J. Mol. Spectrosc. **138,** 141–161 (1989).
65. R. Berman, P. Duggan, P. M. Sinclair, A. D. May, and J. R. Drummond, "Direct measurements of line-mixing coefficients in the $\nu_1+\nu_2$ Q branch of CO_2," J. Mol. Spectrosc. **182,** 350–363 (1997).
66. E. Arié, N. Lacome, P. Arcas, and A. Levy, "Oxygen- and air-broadened linewidths of CO_2," Appl. Opt. **25,** 2584–2591 (1986).
67. L. Rosenmann, J. M. Hartmann, M. Y. Perrin, and J. Taine, "Collisional broadening of CO_2 IR lines. II. Calculations," J. Chem. Phys. **88,** 2999–3006 (1988)